Density, microstructure, and strain-rate effects on the compressive response of polyurethane foams

Kapil Bharadwaj Bhagavathula[a], Christopher S Meredith[d], Simon Ouellet[c], Sikhanda S Satapathy[d], Dan L Romanyk[a,b], James David Hogan[a]

[a]*Department of Mechanical Engineering, The University of Alberta, Edmonton, AB T6G 2R3, Canada*
[b]*School of Dentistry, The University of Alberta, Edmonton, AB T6G 1C9, Canada*
[c]*Valcartier Research Centre, Defence Research and Development Canada, Quebec, G3J1X5, Canada*
[d]*Weapons and Materials Research Directorate, US Army Research Lab, Aberdeen Proving Ground, MD 21005, USA*

Abstract

Background: Foam density, microstructural features (e.g., pores sizes and wall thicknesses), and strain rate have significant influence on the mechanical response of polymeric foams. Objective: The main objective of this study is to study the combined influence of density, microstructure, and strain-rate on compressive response, damage accumulation, and failure mechanisms in polymeric foams. Methods: Microstructural morphological parameters (e.g., pores sizes and wall thicknesses) have been quantified using Micro X-ray tomography and MATLAB-based techniques. Polymeric foam samples were examined under uniaxial compression loading at quasistatic (0.001 to $0.1s^{-1}$), intermediate (1 to $250s^{-1}$), and dynamic strain rates (3200 to $5700s^{-1}$). All experiments were coupled with high speed cameras to measure strain using 2D digital image correlation, and to visualize deformation. Results: The variation of the mechanical properties across all densities (e.g., elastic modulus and collapse stress) are found to behave in a power-law fashion with respect to strain rate. A comprehensive dataset across varied range of densities and strain rates, especially intermediate strain rates is lacking in pre-

Email address: bhagavat@ualberta.ca (Kapil Bharadwaj Bhagavathula)

vious research, and generalized phenomenological relationships developed in this paper to predict combined influences of density, microstructure, and strain-rate over varied range of materials are important contributions of this work. Conclusions: The results showed that the power-law relationships act as a good predictor for the prediction of mechanical properties and elastic response, and as an indicator for damage mechanisms in these polymeric foams.

Keywords: computed tomography, polymeric foam, microstructure, compression, strain rate

---

1. Nomenclature

Foam density	ρ	kg/m^3
Base polymer density	ρ_s	kg/m^3
Relative density	R	-
Porosity	ϕ	-
Foam elastic modulus	E	MPa
Base polymer elastic modulus	E_s	MPa
Characteristic modulus	E_0	MPa
Engineering stress	σ	MPa
Pore collapse strength	σ_{pl}	MPa
Axial strain	ϵ	mm/mm
Strain rate	$\dot{\epsilon}$	s^{-1}
Reference strain rate	$\dot{\epsilon}_0$	s^{-1}
Pore size	D_i	μm
Wall thickness	t_i	μm

2. Introduction

Polymeric foam materials are used to mitigate energy transfer between objects during a varied range of events. These foams are used in a wide range of applications such as military [1, 2], aerospace [1, 3, 4], automotive [3, 4], and packaging applications [2]. Their low densities and energy absorbing capabilities make them an ideal candidate for usage as protection materials, such as in personal protection equipment (PPE) like helmet liner materials [2, 5] and knee pads [5]. In these applications, the foams are often subjected to severe loadings involving multi-axial stress states and dynamic strain rate loading conditions. By gaining a better understanding of the mechanical properties of polymeric foams, higher quality protective equipment materials may be manufactured.

Studies on the use of foams for protective applications have considered a variety of possible materials that could be used in dynamic environments, such as functionally graded foams (FGF)[6], micro-lattice structures[7], and single and bi−layered foams [8]. For example, Cui et al.[6] investigated the properties of FGFs and found that they are more effective at absorbing energy at lower strain rates and are slightly less effective at high strain rates because the foam properties are dominated by the lowest density layers at high strain rates. In a separate study, Schaedler et al.[7] studied micro-lattice structures finding that their energy absorbing capabilities are higher at lower strain rates, although, further investigation is required for higher strain rates. In another study, Fitek et al.[8] compared the peak acceleration responses helmets with different foam liners of a range of densities from 32 to 80 kg/m^3. These foams were studied under both quasistatic and impact loading conditions, and acceleration responses were compared with finite element method (FEM) simulations to make quantitative comparison of compressive response between materials of different densities. From the results in these studies

[6–8], it was observed that the relationship between density, strain rate, and mechanical strengths in these materials are not fully understood.

To characterize foam materials, some authors used energy absorption diagrams, which plots the amount of absorbed energy as a function of the transmitted load [9]. Other authors have investigated in more details the microstructure [10], density [10, 11] and strain rate [10, 11] [5, 12–14], effects on mechanical properties. In their study, Saha et al.[11] discuss the behavior of closed-cell polyurethane and polyvinyl chloride (PVC) foams under compressive dynamic loading conditions and show that PVC foams show a higher degree of strain rate dependency on performance when compared to polyurethane foams. It is observed that in these materials, stress is dependent on combined effects of strain rate, stress state, and mode of failure. In another study, Di Landro et al. [10] observed the effects of density on mechanical response, and found that higher density foams have a higher compressive plateau, so they are able to absorb more energy at constant stress. This may help reduce transmitted load while limiting the load on the structure, compared to a lower density foam, which may densify and end up transferring higher loads. They also observed that higher density foams transmit relatively higher instantaneous acceleration loads, which are often an undesirable type of load transfer in impact applications [8]. A number of other studies aimed at studying density effects have found that higher densities in foams lead to increasing energy absorption with increasing strain rates [5, 11, 15, 16] up to a threshold density and strain rate. For example in one study, Ouellet et al.[12] found this threshold rate to be approximately $1000s^{-1}$, after which the rate sensitivity is observed to change [6, 12].

In addition to efforts made to investigate material responses under different stress states [10, 11, 16, 17], and for a range of density effects [5, 10, 11, 18–20], the sensitivity of mechanical response to microstructure (pore morphology) in foams is also

documented [1, 5, 11, 21, 22]. One way to examine material microstructures is through the use of micro X-ray computed tomography [23] which allows for examination of the internal microstructure of the foam. Micro X-ray computed tomography (XCT) is a widely recognized characterization technique that makes use of computer processed X-ray measurements to reproduce cross−sectional images of internal objects for a range of different materials [1, 24, 25]. By examining the microstructure of the foam material before and/or after experiments, one is able to gain insight into the relationship between foam pore size and wall thickness with the mechanical behavior of the material. This is important because some studies [5, 11] involving foams have compared different microstructures, finding that the smaller pore size generally had higher strengths and absorbed more energy at high strain rates when compared to larger pore sizes. In one example, Bouix et al.[5] also found that changes in the strain rate have smaller effects on foams with smaller pore sizes compared with larger pore sizes. Altogether, these studies point to the importance of the microstructure length scales on the rate-dependent response of polymeric foams.

In the present paper, we seek to explore the effects of density, microstructure (pore size and wall thickness), and strain rate on the mechanical response of polymeric foams. This paper is comprised of the following sections: first, experimental methods are presented that include microstructure characterization techniques, specimen preparation, and mechanical testing. This is followed by the presentation of the experimental results. These results are supported by XCT images, cumulative distribution functions of microstructural features (e.g., pore size), and stress-strain curves. Finally, empirical relationships of mechanical strength parameters are described along with detailed discussion of implications and contributions of the present work with respect to the existing literature.

3. Experimental Methods

The materials investigated in this work are open-cell polyurethane foams that were manufactured by PORON. In this study, foams of three different densities are examined under uniaxial compression loading at quasistatic, intermediate, and dynamic strain rates. The material densities were: 195 kg/m^3 (termed 'low density' or LD throughout for brevity), 244 kg/m^3 (termed 'medium density' or MD) and 405 kg/m^3 (termed 'high density' or HD). The density of the samples is measured through Archimedes principal (weighing and measuring displacement volume) and these measurements match those listed by the supplier, which are obtained using ASTM D 3574-95 Test A standard [26]. The chemical composition of the materials is held proprietary by the manufacturer and some of the physical and mechanical properties provided by the manufacturer are listed in Table 1. Generally, it is observed that strengths increase as the density increases.

Table 1: Physical and mechanical properties of PORON XRD foams provided by the manufacturer [26–28].

Property	Test method	Material		
		LD	MD	HD
Density (specific gravity)	ASTM D 3574-95 Test A	0.14	0.19	0.40
Compressive strength (kPa)	$0.08 s^{-1}$@ 25% deflection	8-23	10-38	69-138
Tear Strength, min. (kN/m)	ASTM D 624 Die C	0.8	0.9	2.5
Tensile Elongation, min. (%)	ASTM D 3574 Test E		$>$145	
Tensile Strength, min. (kPa)	ASTM D 3574 Test E	207	310	483

3.1. Microstructure Characterization

Shown in Figure 1 are the microstructures of the three different density foams. These images are XCT scans of the pristine specimens. Visually comparing the low density

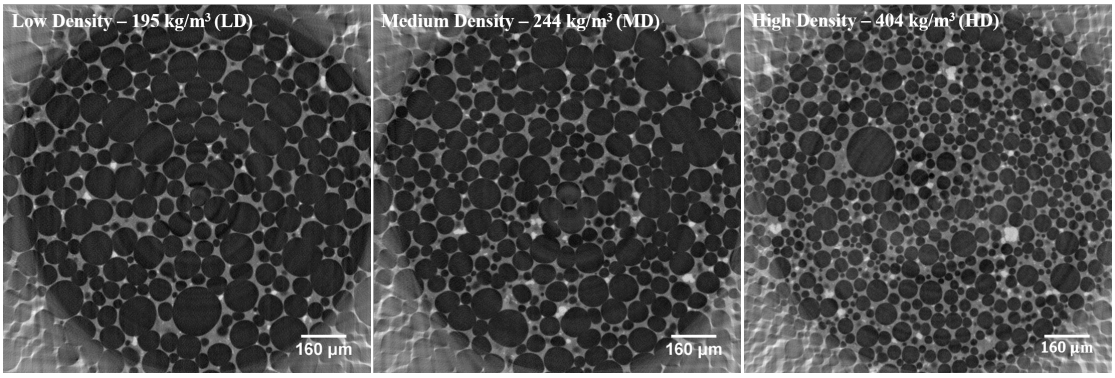

Fig. 1: Pristine microstructures of open-cell polyurethane foams with different densities of $195kg/m^3$(LD), $244kg/m^3$ (MD), and $405kg/m^3$ (HD) obtained from X-ray tomography scans.

foam ($195kg/m^3$) to the high density foam ($405kg/m^3$), differences in pore sizes and the number of pores are noted. It is generally observed from these images that as density decreases the average pore size typically increases, and for a given specimen size, this causes a reduced number of total number of pores available for pore characterization. These characteristics will be quantified later. Conventionally [29, 30], authors classify open-cell foams based on the relative density (ρ/ρ_s) of the foam. In the present study, X-Ray tomography reconstructions are also used to identify the connectivity of the pores to determine whether or not the foam is open- or closed-cell, and it was also found that the ratio of volume of completely closed pores compared to scan volume was relatively low, confirming the macroscopic open-cell nature of the foams.

Synchrotron radiation based X−ray microtomography was performed at the Biomedical Imaging and Therapy (BMIT) facility − Canadian Light Source (CLS)[31] 05ID−2 − SOE−1 hutch, Saskatoon, to obtain volumetric information on the microstructure. The specimens were mounted with their loading axis parallel to the scan direction. The resolution of the scans was $1\mu m$ per voxel and the maximum scan thickness was $5mm$. This resolution provides sufficient scan volume in order to resolve the cell wall thickness

(< 30μm), and pore size (< 250μm) analysis. The specimen loading stage operated in intermittent motion and each specimen scan comprised 900 tomograms being acquired within 10 minutes over a 360° rotation. Reference images without the specimen, and dark images without X-rays were also obtained before and after every scan to increase the quality of images during background filtering reconstruction [32].

Table 2: Microstucture characterization pore metrics

Type	Density (kg/m^3)	Foam thickness (mm)	Average pore size (μm)	Average wall thickness (μm)	Average porosity (ϕ)
LD	195	4.2	60 ± 55	10 ± 9	0.87 ± 0.06
MD	244	3	45 ± 35	11 ± 10	0.83 ± 0.06
HD	404	3	32 ± 30	11 ± 10	0.76 ± 0.05

A MATLAB-based program was developed to perform image segmentation on the XCT slices to calculate pore sizes and wall thicknesses. First, the original grayscale images are imported into an array in MATLAB and stacked over each other. Then, all images are converted to a binary scale with appropriate thresholding (to account for differences in contrast in the XCT scans) so as to identify the pore boundaries and empty spaces between them. This gives the representation of the specimen in the form of a three dimensional matrix containing 1's (denoting solid material) and 0's (denoting empty spaces or voids). The border pores are cropped out to remove the edge artifacts and a cylindrical projection containing pores remains as seen in Figure 2(a). Using a standard MATLAB function called "erosion", the walls are thickened to connect walls that may have been disconnected during image processing or pore scanning, and this produces completely closed pore structures. An example of the resulting image is shown in Figure 2(b). Using the images of the thickened pores shown in Figure 2(b), the cen-

troids of every pore volume are calculated in 3D using the standard "regionprops" function and stored. Next, the coordinates of all the centroids are plotted onto the original 3D binarized stacked images. From these centroids, vectors are drawn in 6 orthogonal directions in $\pm x$, $\pm y$ and $\pm z$ as shown in Figure 2(c). The program then calculates the number of pixels encountered as 0's (within a pore) followed by 1's (as it passes through a pore wall) along these vector directions and these pixel counts are multiplied by appropriate length scale conversions to calculate pore sizes and wall thicknesses. The pore sizes and wall thicknesses for each specimen are then tabulated and stored for further data processing. This type of analysis needs to be performed when working with open-celled microstructures because pore sizes cannot be easily determined like in other material systems like advanced ceramics [33]. Shown in Table 2 are the pore metrics calculated from characterization of the three density foams. The first column shows the type of foam, followed by density, and the as-received sheet thicknesses. The table also shows the average pore size, average wall thickness, and average porosity (ϕ) for all foams. The porosity of the low, medium, and high density foams is measured to be 0.87 ± 0.06, 0.83 ± 0.06, and 0.76 ± 0.05, respectively. These differences in porosity are obtained as a result of different thresholds across difference sample scans. Due to the variation of pore sizes in these materials, the total number of pores characterized for each density varied among each other, and were found to be $\sim$ 1750 pores, $\sim$ 3100 pores, and $\sim$ 9950 pores for the LD, MD, and HD foams, respectively. It is to be noted that the variability in these pore metrics measurements is determined by the thresholding limits from the reconstruction. To explore the repeatability of the results, the initial stack of images were rotated by various degrees and the analysis was carried out on these images. Pore size and wall thickness distributions were found to be equivalent to when performing these operations on the original image stack.

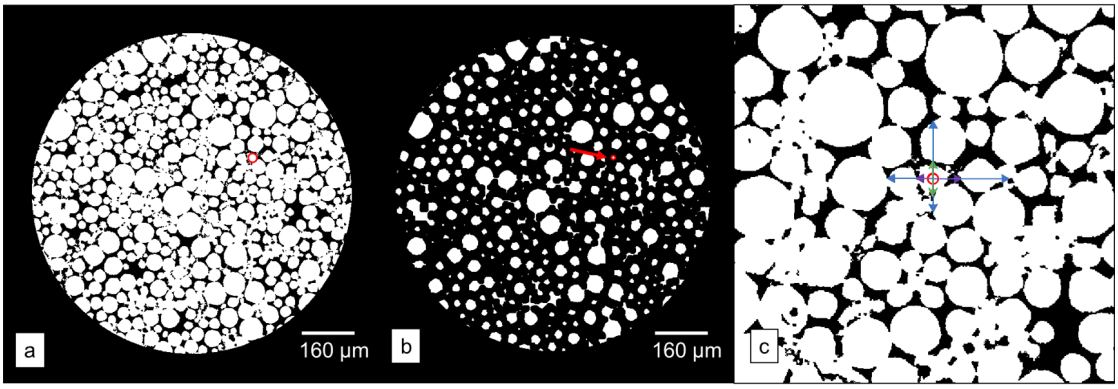

Fig. 2: Microstructure characterization methods (a) Binarized image of foam scan with border pores cropped out. (b) Thickened walls to identify pore centroids. (c) Zoomed view of a single pore shown with red arrow from (b) showing orthogonal vectors extended from pore centroids to calculate pore size and wall thickness.

3.2. Specimen Preparation for Mechanical Testing

To ensure consistency across strain-rates in compression testing, a single specimen diameter was used for both quasistatic, intermediate, and dynamic experiments. Using a special metallic hollow punch, disk specimens of diameter $8.0 \pm 0.3mm$ were cut from an as-received sheet of uniform thickness of 4.2 mm, 3.0 mm, and 3.0 mm for the LD, MD, and HD foams, respectively, with the axis of the cylindrical disk oriented along the through-thickness direction of the as-received sheet of foam. Care was taken to ensure that the end surfaces of the specimens were parallel, and that minimum damage was induced to the edges during specimen preparation. The sensitivity of material strengths to geometry, testing methods, and specimen-size effects are widely discussed in literature [14, 34]. We note that differences in the compressive strengths between this study and those provided by the manufacturer is expected because the specimen sizes used in the ASTM D3574-95A standard [26] is cuboidal shape with a dimensions of 380 mm x 380 mm x 100 mm, whereas the test specimen size in our study is cylindrical shape with 8 mm diameter and thickness was governed by the thickness of the as-received

foam sheets. The sample geometries were selected based on as-received sheets, ability to compress to sufficient densification strains based on available experimental setups, to have consistent sample sizes across test setups, and to achieve reasonable strain rates and force equilibrium. These samples are similar sizes to those in the literature [1, 35]. We note that potential differences in composition, pore size, and wall thicknesses may also occur as a result of different sizes of as−received sheets than those that are reported by the manufacturer.

3.3. Quasistatic Compression Experiments

The specimens were tested in quasistatic compression at strain rates of 0.001 to $0.1s^{-1}$ using an Instron E3000 material testing system. A 3 kN load cell with a background noise corresponding to approximately ±0.01 N recorded the time histories of the forces, and the displacement of the piston was measured to an accuracy of 0.001 mm using a linear variable differential transformer displacement sensor. The load cell resolution is sufficient to capture the necessary trends in the force measurement needed to properly assess the elastic properties. The engineering stresses are calculated by dividing the applied load by the original specimen surface area, and the engineering strains are computed using digital image correlation (DIC) using a high-speed AOS PROMON U750 camera. DIC methods are discussed in a later sub-section. Three trials with the same loading conditions were performed to verify repeatability of the material behavior.

3.4. Intermediate Compression Experiments

Intermediate strain rate compression experiments were performed at two rates using different loading techniques. The first strain rate, $1s^{-1}$, utilized an Instron 8871 load frame at displacement rates of 3 mm/s for MD and HD foams and 4.2 mm/s for LD foams, corresponding to the sample thicknesses. A 1 kN load cell with a background

noise corresponding to approximately ±0.01 N recorded the time histories of the forces. The deformation of the sample was recorded with a FLIR Grasshopper 3 camera at $164 fps$ with a $200mm$ macro lens. Both the force measurement and image capturing was controlled by the DIC software to ensure the data were time-synchronized. The sample surface was illuminated with a halogen fiber optic light that ensured good brightness even at high strains.

The second intermediate rate was approximately 175 to $250 s^{-1}$ and utilized a drop tower to reach the necessary velocity. A force sensor was attached to a steel base plate, and the sensor had a metal loading cap screwed into it that transmitted the force to the quartz sensing element inside the sensor. The foam sample was placed on the loading cap. A tup, that is the metal rod is positioned above the sample, and dropped to load the sample. The tup is relatively heavy ($\sim$ 4.5 kg) compared to the foams and so the velocity is nominally constant over the majority of the loading time. The slowest velocity achievable was programmed into the drop tower software ($770 mm/s$), corresponding to a drop height of approximately $25mm$ above the sample. The force sensor was a PCB 200B04 with a capacity of $4.45kN$ and an upper frequency limit of $75kHz$. The voltage output of the force sensor was measured with an oscilloscope that was triggered on the rise of the sensor output following impact. The sample deformation was recorded with an iX716 high speed camera at $20,000 fps$ and an exposure time of $20\mu s$ with a $200mm$ macro lens. When the scope triggered, a trigger signal was sent to the camera. In order to time-synchronize the force and camera framing, the camera exposures were sent to the oscilloscope and were also recorded. The samples were illuminated with multiple halogen fiber optic lights to ensure optimum brightness and contrast.

For the intermediate compression tests, the engineering stresses were calculated by dividing the applied load by the original sample area, and the engineering strains were

computed using DIC software. At least three tests with the same loading conditions were performed to verify the repeatability of the foam behavior.

3.5. Dynamic Compression Experiments

The dynamic compression experiments were performed using a split-Hopkinson pressure bar (SHPB) apparatus with bars that were made of solid Aluminum (Al). The SHPB apparatus consists of a projectile launcher, a striker bar (Al), an incident bar (Al), and a transmission bar (Al). In a SHPB experiment, a striker bar is launched from the projectile launcher and strikes the incident bar, generating an elastic stress wave that travels through the incident bar and through the specimen, dynamically loading it. Due to the mismatch of mechanical impedances of the bar material and the foam specimen, mechanical waves are generated at either end faces of the specimen. Two strain gages are mounted on diametrically opposite sides of the incident bar, and the transmission bar via a bridge configuration, to record these mechanical waves as strain histories, and they are connected to a data acquisition system. The strain gages had a resistance of $350 \pm 0.3\%$ with a gage factor of $2.130 \pm 0.5\%$ (Micro Measurements CEA-13-250UN-350 semiconductor strain gages). Each strain gage set was connected to an individual conditional amplifier (Vishay InterTechnology 2310B), and a gain of $\sim$ 100 to 1000 is applied on the transmission gage signal because of the small magnitudes of transmitted pulses. The output from the conditional amplifiers is saved to an HBM Gen3i High-Speed Recorder at a sampling rate of 25 MHz. The background noise in these strain measurements was $\approx \pm 1$ micro strain, and was found from careful observation of transmitted gage raw voltage data. The 1 micro strain corresponds to $\sim$ 20% of the measured strain at the onset of yielding ($\sim$ 5 micro strain). The lengths of incident bar and transmission bars were 1000 and 910 mm respectively, with a diameter of 12.7 mm.

A 500 mm long solid flat-ended projectile with a similar diameter was used in this study to generate a top-hat loading profile. The length of the bars and the relative positioning of strain gages avoided overlapping of the stress waves [36], also ensuring that longer loading durations are available in order to obtain larger strains. A 160 GSM paper was used as a pulse shaper for the dynamic experiments, and this was selected after multiple trial and error methods were pursued using different pulse shapers. Paper pulse shaper was also used in other studies in literature [37]. The use of a paper pulse shaper did not change the rise time but helped reduce high frequency noise in the input wave, as well provided acceptable force equilibrium. The controlled deformation of the pulse shaper generates the desired loading profile of the input pulse that is a flat top hat, and this ensures constant deformation rate in the specimen under dynamically equilibrated stress conditions [38]. In our SHPB experiments, the engineering stress is calculated from the transmitted strain-time history [39, 40].

In the present study, the dynamic compression experiments were coupled with an ultra-high-speed Shimadzu HPV-X2 camera to visualize deformation features, as well as to perform strain measurements using DIC. The dynamic stress equilibrium in the specimens was verified by comparing the forces at input bar-specimen and specimen-transmission bar interfaces, and the force curves indicated that reasonable force equilibrium was attained within the specimen. Example figures of force balance curves and filtering of the dynamic stress-strain curves are provided by the authors in Bhagavathula et al.[41]. The challenges of developing SHPB systems to accurately measure the dynamic response of foams are well documented in the literature [5, 11, 15, 16, 42], and the testing methods that are pursued in the present study are consistent with those in the literature.

3.6. Digital Image Correlation (DIC)

DIC is used to measure the strain during experiments in all experiments. DIC is a non-contact full-field quantitative strain measurement technique that allows the determination of in-plane displacement components, and therefore the surface strain fields experienced by the specimen during loading [23]. Imaging of specimen surface was conducted in all experiments to provide images for DIC. As mentioned earlier, the quasistatic testing setup was coupled with a high-speed camera AOS PROMON U750 which provides a resolution of 1280 x 1024 pixels and recorded at a frame rate of 100 frames per second. A FLIR Grasshopper 3 camera at 164 fps was used to record the $1s^{-1}$ intermediate compression experiments, and an iX716 high speed camera at $20,000fps$ was used for the 175 to $250s^{-1}$ intermediate compression experiments. In the dynamic compression experiments, the ultra-high-speed camera Shimadzu HPV-X2 camera captured 256 images for each experiment and is triggered by a split signal from the incident strain gage. In dynamic experiments, the ultra-high-speed camera operated at a framerate of 1 million frames per second at a resolution of 400 x 250 pixels. The camera output pulses were used to correlate times between the images and the strain gage measurements. All cameras were equipped with a telecentric lens to eliminate out-of-plane motion capture. The naturally occurring microstructural pore texture of the surface of the specimen was too small to be captured using the available pixels and hence all specimens were coated with black paint using an ultra-fine point Harder and Steenbeck Infinity airbrush to form a speckle pattern on the specimen surface for accurate correlation purposes. A sample speckle pattern is shown in Figure 3(a) for quasistatic compression experiment of PORON HD at $1s^{-1}$.

These camera images are used for DIC strain measurements using the VIC-2D 6 software [43]. In DIC analysis, a region of interest (ROI) is defined on the sample sur-

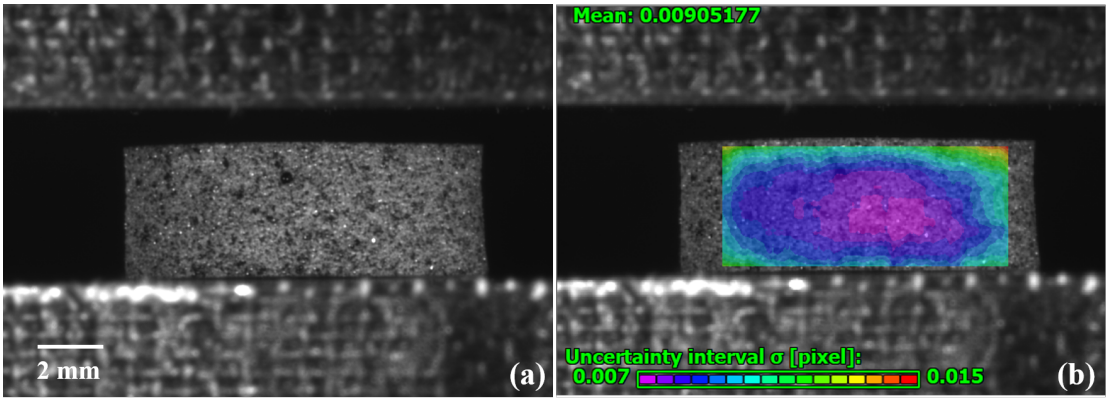

Fig. 3: (a) Speckle pattern on prepared cylindrical specimen (b) Region of interest used to compute strains using digital image correlation.

face, and displacements of all the subsets defined within the ROI are tracked as the specimen deforms during loading. In each displacement step, the subsets in the deformed images are "matched" with the pattern in the reference image using the difference in gray scale intensity levels at each interpolation point. In each subset, a correlation peak is defined by interpolating the grayscale level at or between pixels, and the position of the peak provides a local displacement [44]. For these measurements, the optimum settings of the brightness and contrast on the material surface is obtained by using a combination of high intensity LEDs and speckle patterns. The system was adjusted for every specimen such that images with good sharpness and exposure are obtained which provided an optimal subset size in the VIC-2D 6 software. The software's built-in algorithm provides a "suggested subset size" and noise level with the minimum estimated error that is based on the quality of speckle pattern and contrast level using the reference image. An example ROI used for DIC measurements is shown in Figure 3(b) and the noise level was found be to < 0.01 in all the experiments. For the large deformations experienced during compression, incremental DIC is utilized to avoid de-correlation,

which uses the image of the previous displacement step as the reference image for correlating the positions of the speckles in the next displacement step. It is to be noted that the primary interest in this paper is to measure the axial strain experienced by the specimens, and 2D DIC allows for the accurate measurement of this strain [45].

4. Experimental Results

4.1. Microstructure Characterization

4.1.1. Pore size characterization

By visualizing the pore size data (or wall thickness data) in an empirical distribution function (eCDF), insights can be gained as to what pore size length scales are activated during testing. The cumulative distribution [46] is defined as:

$$G(x) = \int_0^x g(\bar{x}) d\bar{x} \tag{1}$$

where $g(\bar{x})$ is the probability distribution of the pore sizes. The pore size data set in each direction is a discrete set of n pores with sizes of ℓ_i (i=1...n). Ordering this data for increasing pore size, and assigning a probability of $1/n$ to each pore, the normalized empirical cumulative distribution function can be computed as the sum of these probabilities:

$$G_e(\ell) = \frac{1}{n} \sum_{i=1}^{n} I(\ell_i \leq \ell) \tag{2}$$

where the indicator function I has a value of 1 if $\ell_i \leq \ell$ and 0 otherwise. Pores with sizes less than $250\mu m$ were considered for further analysis based on visual confirmation from the XCT scans (Figure 1). Orthogonal scans in the z direction were also obtained and the pore size distribution in the z direction was found similar to that of the x direction, enabling us to compare cumulative distribution of pore size in x and y directions. Shown

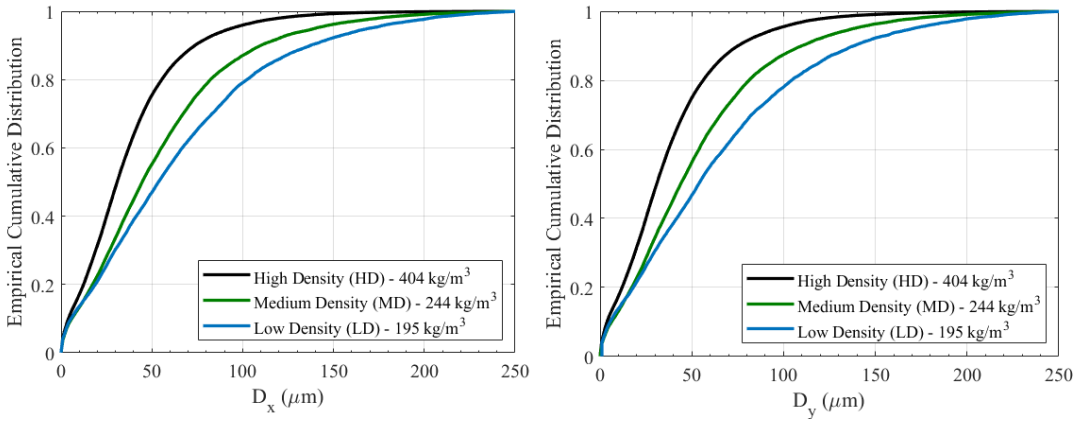

Fig. 4: Empirical distribution functions showing pore sizes of different density foams in both x and y directions. The black, green and blue curves represent the high density (HD), medium density (MD), and low density (LD) foams, respectively. Pore size eCDFs appears to shift left as density increases.

in Figure 4 are the eCDFs which are used to identify the likely range of the pore sizes and trends, where D_x and D_y represent the pore diameters in x and y directions, respectively. This is achieved by looking at the values between the 10th and 90th percentiles. It is observed that the different density foams have varied sizes in the x and y directions. For the low density foam, the limits lie between $5-114\mu m$ for the x, and $6-142\mu m$ for the y directions. For the medium density foam, the limits lie between $6-100\mu m$, and $8-110\mu m$ for the x and y directions, respectively. For the high density foam, the pore sizes are found to be near spherical in nature with limits ranging from $5-75\mu m$ for both x and y directions. Generally, the eCDF shifts to the right as the density decreases, and this indicates that pore sizes are larger in the lower density foams. The eCDF curves also reveal that the the sizes for D_x is greater than D_y, and this is likely a result of the foaming direction during the manufacturing process.

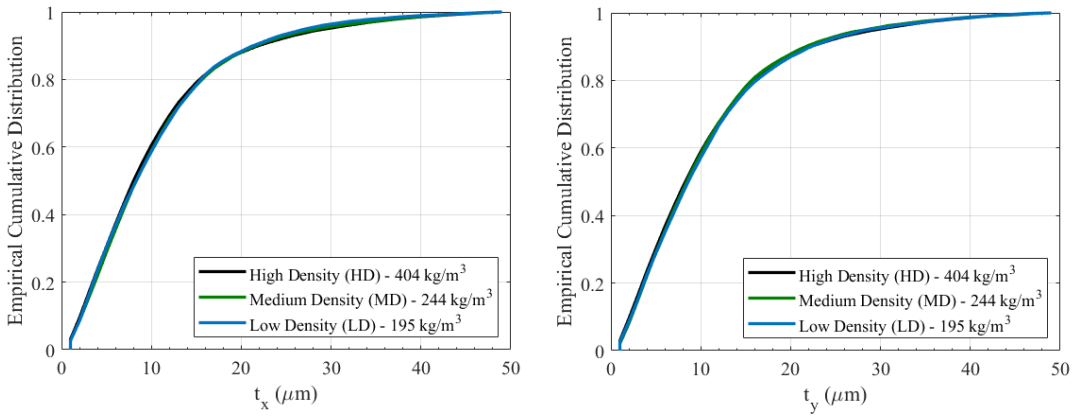

Fig. 5: Empirical distribution functions showing wall thicknesses of different density foams in both x and y directions. The black, green and blue curves represent the high density (HD), medium density (MD), and low density (LD) foams, respectively. Wall thickness eCDFs appears to be similar for all densities.

4.1.2. Wall thickness characterization

Shown in Figure 5 are the eCDFs of the wall thicknesses for all the different foams. Wall thickness less than $50\mu m$ were considered based on visual confirmation from XCT images (Figure 1). In Figure 5, t_x and t_y represent the wall thicknesses in x and y directions, respectively. The wall thickness range is measeured to be between $2\mu m$ and $23\mu m$ in both x and y directions for the pristine specimens, and it is is observed that profiles of t_x and t_y are similar for all the different density foams. These observations are made from looking at individual plots of each specimen with t_x and t_y on the same plot. Although relative differences between the different density foams are minor ($< 1\mu m$), these minor differences in wall thickness are to be noted.

4.2. Compression Experiments Results

The stress-strain responses of the different density PORON foams at quasistatic, intermediate, and dynamic strain rates are shown in Figure 6. The y-axis represents stress in megapascals in a logarithmic scale and the x-axis represents engineering strain.

It is to be noted that three trials for each experiment were performed for repeatability and representative curves are shown.

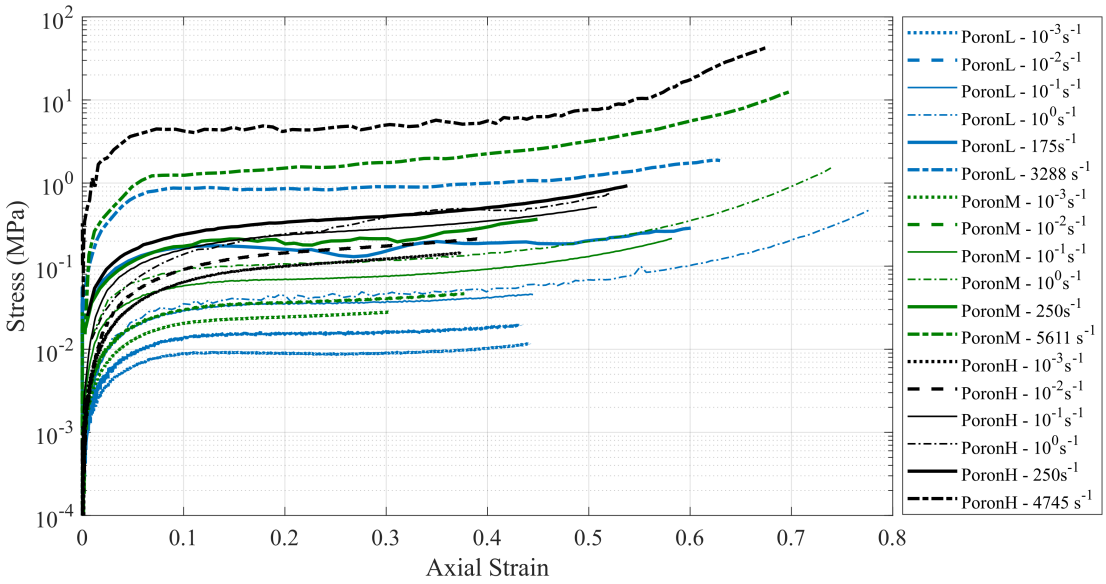

Fig. 6: Figure showing the representative stress-strain responses under quasistatic, intermediate, and dynamic compression for different density PORON foams. The blue, green and black curves represent the low density, medium density, and high density foams, respectively. The different strain rates are represented by separate line styles as shown in the legend.

All curves show three stress regimes, namely, *elastic behavior* up to a yield or *collapse* stress (σ_{pl}), a *plateau* stress regime where the stress is near constant, and a *densification* regime where stress increases rapidly with increasing strain [5, 11, 23, 47]. In this paper, due to differences when DIC correlation is lost, different maximum strains were obtained throughout the experiments. From Figure 6, it is observed that the compressive response of the PORON foams in all the strain rate regimes exhibit a typical elastomeric foam behavior with some minor differences. Namely, typical foam responses have a sudden change in slope when the stress reaches the elastic stress limit and its value is easily identifiable [14, 34, 38]. For all the different densities, it was found that there was a gradual transition from the elastic regime to the plateau regime beginning at a

strain of ~ 0.02 and plateauing at approximately 0.08 strain, which marks the range of yield strain for this material. Polymeric foams have a pore collapse stress (σ_{pl}, stress at 0.25 strain) which represent the stress when foams start to deform post elastic limit when loaded beyond the linear-elastic regime. The collapse of the pore structures gives a long, approximately horizontal plateau to the stress-strain response, where the strain is partially recoverable and some permanent deformation is observed to the foam microstructure post-experiment. In this study. the elastic modulus and the pore collapse stress across the varied strain rates for the different density foams are tabulated in Table 4.2. Comparing the collapse stress between the quasistatic and dynamic strain rates, the dynamic values are anywhere from 70 to 90 times the quasistatic values and, in the case of the elastic modulus, the dynamic ones are higher by 100 to 150 times.

Table 3: Elastic modulus and pore collapse strengths of PORON foams at quasistatic, intermediate, and dynamic strain rates.

	Elastic modulus (MPa)			Collapse stress (kPa)		
Strain rate	LD	MD	HD	LD	MD	HD
0.001	0.12±0.01	0.23±0.02	0.62±0.01	7.78±0.75	17.19±2.51	65.38±0.68
0.01	0.27±0.01	0.42±0.04	0.79±0.03	15.07±0.61	29.63±1.11	90.13±1.24
0.1	0.52±0.04	0.94±0.01	1.65±0.20	29.97±0.76	56.58±3.22	159.17±1.84
1	0.77±0.04	1.73±0.11	4.37±0.63	55.51±0.72	93.77±2.72	276.72±29.39
175	3.62±0.43			243.12±21.22		
250		9.32±0.39	25.06±2.62		491.95±56.98	1738.84±171.94
3275±840	14.19±4.71			669.56 ±112.71		
4577±1117		23.71±5.31			1344.67±159.41	
4307±1330			92.07±29.64			4629.54±447.25

5. Discussion

In this section, first, the discussion on microstructure characterization along with its implications for modeling are presented, followed by the discussion of effects of density, and strain rate on mechanical response of these foam materials. Here, the deformation mechanisms associated with the different deformation regimes are discussed. The damage and failure mechanisms described here are directly dependent on the foam microstructural length-scales [30] such as pore size and wall thickness, and measuring these parameters would help for accurate modeling of material damage at the microstructure length-scale. The mechanisms described here mostly presents the response of foam under compressive loading applied in the rise direction where the cell walls take the bulk of the load during compression, and also applies to all the experiments performed in this paper.

All three foams of different densities in this study have similar stress-strain behavior: an elastic response followed by a plateau stress stage. However, some differences can be noticed between the strain rates and densities in the experiments in this paper. For example, in quasistatic loading, the medium and the high density foam shows a collapse stress of ~ 4 and ~ 5 times larger as compared to the low density foam, respectively. For the dynamic results, all foams do not show a distinct post-collapse hardening transition that is common in PVC foams [11], and polystyrene foams [5], but rather demonstrate a larger length of the plateau stress regime that is different from what is observed in quasistatic loading conditions. When the specimen is loaded beyond the collapse stress, it is expected that larger pores get collapsed initially because of susceptibility of buckling of longer structures (cell walls) [1], and as straining continues, there will be fewer of the large pores since they are being crushed out. As the strain increases,

the average pore size decreases due to crushing out of the porosity and pore collapse of larger pores, which results in an increase in stress. At small pore sizes, post-collapse hardening occurs due to a combination of bending, axial deformation, and other forms of deformation like plastic deformation [30, 48]. In the tests in this paper, it is noted that the plateau stress and elongation of the plateau regime are found to be higher for dynamic strain rates. This indicates that pore collapse increases with increasing strain rate [38] and, hence, the energy absorption capabilities are improved at higher strain rates [38, 49]. In the following sub-sections, these phenomenon and the results presented in the previous section are discussed in further detail and compared to existing data in the literature.

5.1. Microstructure Characterization and Implications for Modelling

From the Figures 4 and 5, it is observed that the pore size decreases with increasing density, whereas there is no discernible change in wall thickness with a change in density. Knowledge of the microstructure pore size and wall thickness is important because these microstructure differences are related to the mechanical responses [11, 38, 50] and performance [5, 51] of foams. For example, it is known that smaller pore sizes are less prone to buckling which results in higher collapse stresses [52], which is observed in the present study in the HD foam which has the smallest pores and the highest collapse stress. In addition, it is also observed in literature that as pore size decreases, the cell walls become more susceptible to micro-inertia effects [5, 34, 52]. Finally, it is to be noted that micro-inertia effects are greater in the case of dynamic loadings, but also when the foam density increases [5]. This has implications for material design in impact applications such as for foams in the present study, where the HD foam is observed to have the highest elastic and collapse stress magnitudes and the smallest average pore

size of all the three density foams, and the mechanical strengths are observed to increase with increasing strain rate. These observations in the present study are consistent with the literature [5, 18, 34, 51, 52].

Further, from the porosity measurements discussed in this paper, a linear relationship within 1% error was found to exist between the pore solid content $(1-\phi)$ and the density (ρ) of the foams give by:

$$1 - \phi = A * \rho \tag{3}$$

where the value of ϕ varies from 0 to 1, and when $\phi = 0$, $\rho = \rho_s$. From a curve fit, the value of A is found to be equal to $8 * 10^{-4}$ for the PORON foams and the density of solid polyurethane polymer at $\phi = 0$ was calculated to be $\rho_s \approx 1250 kg/m^3$. This value is close to existing data in literature for open-cell flexible polyurethane foams [30] where the elastic modulus of the solid polymer material at quasistatic strain rate is given as $E_s = 45MPa$ [30]. This value of E_s will be further used to develop other empirical relationships later in the Discussion section. Similar relationships are discussed by Brydon et al.[51] in their paper where they relate porosity, and volume of the bulk and parent polymer in an effort to determine the incompressible porosity of foam materials during compression.

Next, we explore the modeling implications of probing the foam microstructure and discuss the necessity and advantages of including real microstructures in material models. This is accomplished through comparing pore sizes of foams of different relative densities. Shown in Figure 7 are some existing trends [23, 29, 53] of pore sizes of varying density polyurethane foams with relative densities ($R = \rho/\rho_s$) (ρ_s - base polymer density) less than 0.25, plotted along with data in the present study. Shown in Figure 7 is a plot of average pore size vs. relative density, and both open- and closed-cell

foams are considered for comparison. This data was obtained from published values in the literature [23, 29, 53], where average pore size and foam relative densities were reported. Additional data exists in the form of images in other studies [9, 48, 54] but often only one figure is presented, and it is therefore difficult to extrapolate average pore sizes from them. It is to be noted that the foams used in these studies might have different base chemical compositions or the presence of certain additive particles during foaming processes [41, 42], and this contributes to the observed variation in pore sizes in the foams. Generally from Figure 7, it is observed that overall pore size decreases with increasing relative density. It is also observed that at a similar relative density, closed-cell foams have relatively bigger pore sizes when compared to open-cell foams. For the foams in this study, it is observed that both the average pore sizes and pore size variability decreases with increasing relative density. In their study, Jarfelt et al.[29] measure pore sizes of different density foams to aid in thermal conductivity calculations of foam materials. In another study, Mills et al.[53] note the differences in microstructures with respect to closed-pore content, pore orientation and spacing, and pore size, and relate these parameters to foam manufacturing processes. Generally, one of the common implications of many of these studies in literature focused on characterization[29, 53, 55–57] is the necessity of including such measurements of real microstructures in micro-mechanical modeling approaches to improve existing models, and we hope our data contributes to those studies.

Finally, in the existing literature, numerical models [51, 58–60] have been developed for polymeric foams to predict the behavior of open-cell foam materials under compressive loading. In some models in the literature, the loading directions are arbitrary to the foam rise direction [58, 60], and in that case, it is observed that models do not necessarily capture the effects of microstructure. It is also observed that micro-mechanical

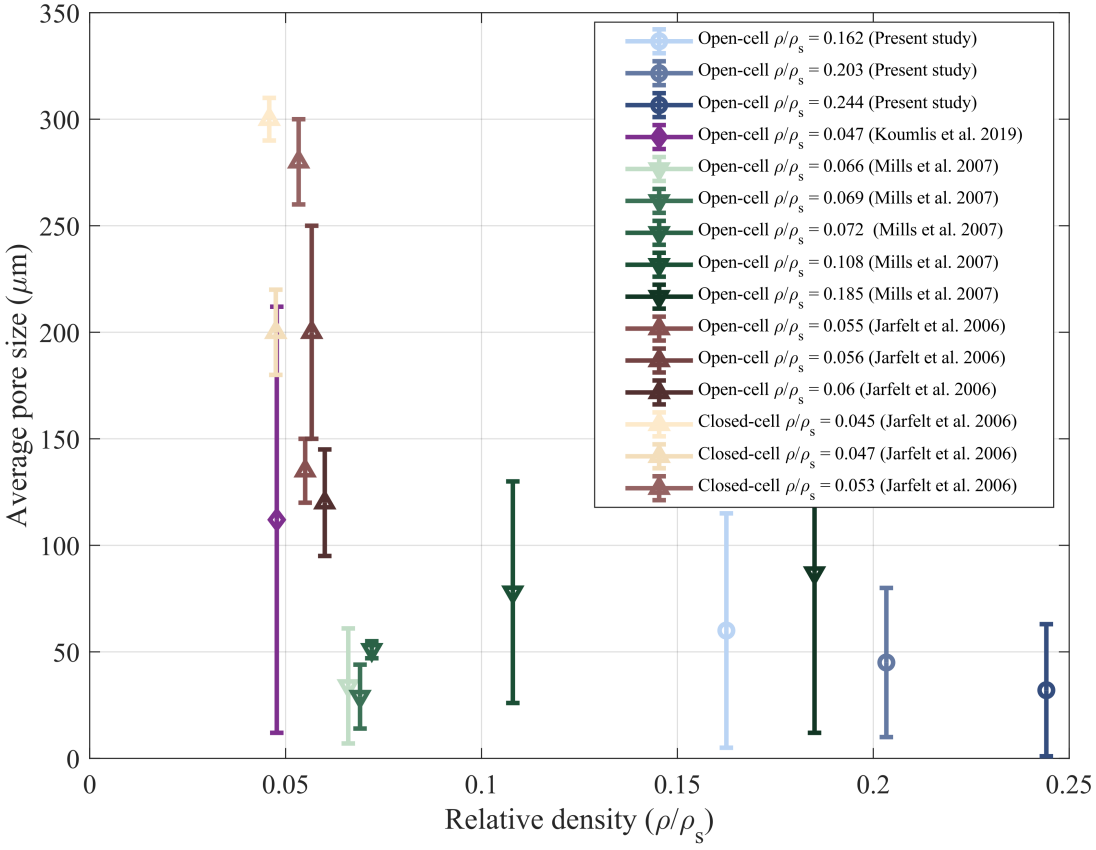

Fig. 7: Trends of average pore sizes of varying density open-cell and closed-cell polyurethane foams with different chemical compositions/additives for foams with relative density less than 0.25. Data in the legend is ordered based on relative density for a given study.

models based on idealized foam microstructures of either ordered[59, 61] or random network[49, 58, 59] of pores may not always reflect the experimental data accurately in one particular loading direction [58, 59]. Further, it is to be noted that the structural response of foams is also governed by the cell geometry (cell topology, foam density and anisotropy ratio) and by properties of the base polymer material [53]. Existing research on open-cell foams have also considered a wide range of pore microstructures, including polyhedrons, truncated octahedrons and rhombic dodecahedrons [58]. Many studies [47, 51, 53, 59] note a necessity of including these length scales in the constitu-

tive models to better predict material response. This can be achieved by generating unit cells based on statistics of real microstructural parameters [55] of foams such as closed-pore content, pore size and wall thickness, and the pore orientation and spacing. One of the identified contributions of the present study is that the characterization techniques provided in the present study can be employed directly, or improved upon, to identify such statistics of foam microstructures to enable better micro-mechanical modeling.

5.2. Effect of Density on Compressive Response

As seen from Figure 6, the collapse stress, peak stress and plateau stress increase with increasing material density. It is also observed from the figure that the span of the plateau stress regime decreases with increase in foam density. From measurements, it was observed that the initial stiffness increases with increase in foam density. To relate the mechanical properties and relative density of the polymeric foams, power-law relationships are commonly defined in the literature (e.g., closed-cell polymeric foams [11] and open-cell foams [30]):

$$\sigma_{pl}/E_s = B(\rho/\rho_s)^m \tag{4}$$

where $\sigma_{pl}(MPa)$ is the collapse stress of the foam, $E_s(MPa)$ and $\rho_s(kg/m^3)$ are the elastic modulus and density of the solid base polymer material, respectively, and B and m are empirical fitting parameters. Gibson and Ashby [30] had initially developed a very similar expression based on micro-mechanical formulations for various low density foams and found that $\sigma_{pl}/E_s \approx (\rho/\rho_s)^{1.5}$ for open-cell foams and $\sigma_{pl}/E_s \approx (\rho/\rho_s)^2$ for closed-cell foams. In a more recent study, Saha et al.[11] found that the power law constants change with loading conditions and found m to vary between 1.4-1.69 for a strain rate range of 0.001 to $1600s^{-1}$. From both existing published data and the

data in this study (Table 4), the power law coefficients appear to be rate-dependent, and different for foams made of different base materials, with m being increasingly more rate-dependent for higher strain rates. The value of the pre-multiplying term B is hypothesized to depend on parameters like: open or closed cells, porosity, microstructure length scales (wall thickness and pore size), and the constituent material [30]. Overall, we note due to the differences in base material, pore structure, strain rate, and loading conditions, that power-law fits to describe density effects are not suitable for a wide range of strain rates. Next, we explore some ideas on stress scaling to predict collapse stress as a function of strain rate in these materials.

5.3. Effect of Strain Rate on Compressive Response

In this subsection, we compile mechanical property data from various open-cell [23] and closed-cell [11, 12, 57] foams, and compare those with our own. This data is used to make appropriate comparisons wherever possible, but is mainly shown to denote magnitude differences between materials. To assess the effect of the strain rate and density on mechanical response, parameters of elastic modulus and collapse stress are identified from the experimental results in this paper. The collapse stress and elastic modulus values were plotted as a function of strain rate for a range of foam densities, along with data from existing literature, in Figures 8 and 9. Shown in Figure 8 is the comparison of elastic modulus of polyurethane foams of varying densities with varying strain rate. From Figure 8, for open-cell foams in the literature [23], and in this study, it is observed that elastic modulus increases with foam density and this relationship is even more pronounced at higher strain rates. For the closed-cell foams in the literature [11, 12, 57], the elastic modulus is observed to increase with increasing foam density and strain rate.

Next, shown in Figure 9 is the comparison of collapse stress of polymeric foams of different densities [11, 12, 23] with varying strain rate. From the figure, the collapse stress is observed to increase with increasing foam density and strain rate, with higher strain rate dependency for open-cell foams when compared to closed-cell foams. In this paper, it is found that a power-law fit best describes the relationships between elastic modulus and, collapse stress, and strain rate:

$$P(\dot{\epsilon}) = C\dot{\epsilon}^{\alpha} \tag{5}$$

where $P(\dot{\epsilon})$ is the measured parameter (elastic modulus or collapse stress), C is the scaling coefficient, $\dot{\epsilon}$ is the strain rate and α is the power-law exponent. The coefficients for all the 3 different densities and other foams in the literature are tabulated in Table 4, and determined using a least squares fit. It is to be noted that these coefficients were calculated based on measurements taken for 6 different strain rates along with 3 repeated measurements for each sample at each rate (total 18 tests per density). Generally, from Table 4 it is found that the elastic modulus and collapse stress have a scaling exponent of ~ 0.3. This is believed to be associated with the dominant damage mechanism across these rates, which is believed to be cell wall buckling [62]. In other published literature [13, 23, 38], various models using logarithmic relationships were proposed:

$$P(\dot{\epsilon}) = P(\dot{\epsilon_0})(1 + klog_{10}(\epsilon/\dot{\epsilon_0})) \tag{6}$$

where $P(\dot{\epsilon})$ describes the effect of strain rate on various parameters like elastic modulus, collapse stress and energy absorption, k is a constant, and $\dot{\epsilon_0}$ is the reference strain rate. Such relationships have been used to describe both open-cell, and closed-cell foams

[13, 23, 38] in the literature but this form did not fit our experimental data and so the power law form was pursued.

Next, to further generalize the pore collapse strength results, we propose a scaling, or normalizing function motivated by previously chosen forms [63]:

$$\frac{\sigma_{pl}}{E_0} = D\left(\frac{\dot{\epsilon}}{\dot{\epsilon}_0}\right)^{\beta} \tag{7}$$

where σ_{pl} (MPa) is the pore collapse stress and D is a scaling coefficient. E_0(MPa) is a characteristic modulus of the foam that is dependent on the dominant damage mechanism in the material (e.g., buckling [62]). In this case, we take E_0 as the Elastic modulus of the foam at the lowest strain rate in this study, viewed as the characteristic stiffness of the foam. Attempts were made to utilize existing analytical solutions for the Young's modulus of unit cells [53, 55, 64], but sufficient scaling was not achieved, likely a consequence of the oversimplification of a unit cell approach in our foam with spatially distributed pore sizes in both open- and closed-cell configurations. A computational

Table 4: Power-law coefficients for elastic modulus and collapse stress for polymeric foams.

Material	Density (kg/m^3)	Elastic modulus		Collapse stress		Reference
		C	α	C	α	
Poron LD	195	1.06	0.32	0.06	0.29	Current study
Poron MD	244	1.81	0.30	0.11	0.29	Current study
Poron HD	404	4.69	0.34	0.36	0.29	Current study
EPS	61	14.84	0.01	0.90	0.024	Ouellet et al. 2006
EPS	120	22.10	0.08	2.49	0.06	Ouellet et al. 2006
HDPE	80	2.71	0.03	0.64	0.038	Ouellet et al. 2006
HDPE	110	5.08	0.02	1.05	0.03	Ouellet et al. 2006
PU	57	0.91	0.24	1.40	0.11	Koumlis et al. 2019
PU	320	87.68	0.07	5.22	0.09	Tang et al. 2017

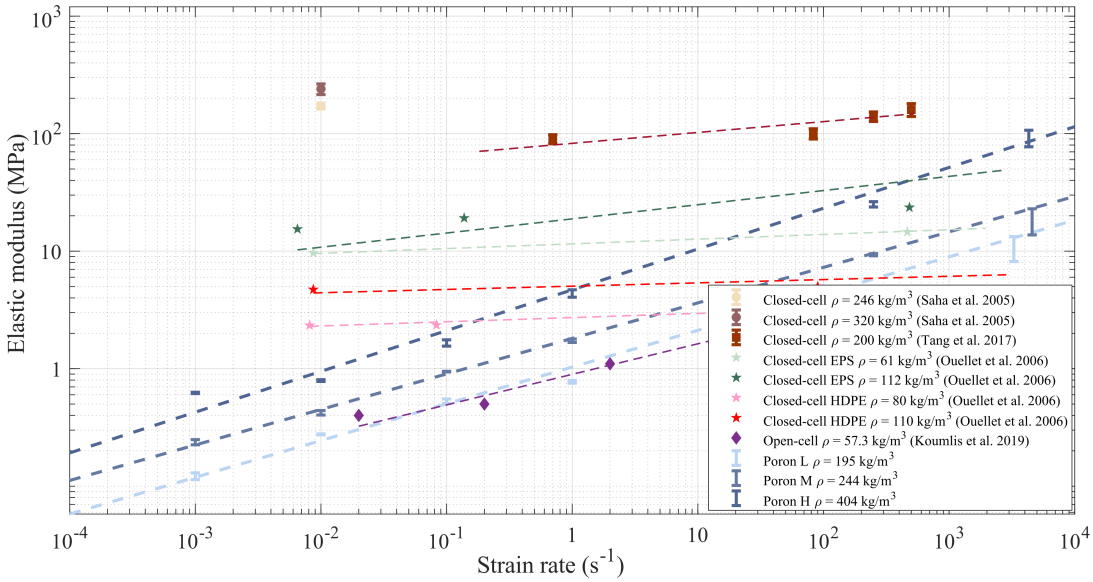

Fig. 8: Trends of elastic modulus of different density foams with varying strain rates under compression loading. Data is ordered based on increasing density for a given study for open-cell foams, followed by closed cell foams. The y axis denotes the elastic modulus (MPa), and the x axis represents strain rate (s^{-1}), and both the axes are represented in a logarithmic scale

modelling approach with unit cells is likely needed to unravel the solution for E_0.

Next, $\dot{\epsilon}_0(s^{-1})$ is a characteristic strain rate in equation (7). This rate is a function of the dominant mechanism over the rates that are being normalized, geometry, and material properties of the foam. The term explicitly accounts for an inherent time scale in the deformation problem. To define this parameter, existing studies in literature have considered timescales associated with damage mechanisms across varying strain rates. In one study, Deschanel et al. [65] used the timescale associated with rupture during creep tests performed on polyurethane foams. In other studies considering high rate loading conditions such as shock and impact [66–68], the authors discuss that the critical length and time scales associated with the respective deformation mechanisms depend on both the intrinsic material properties (dependent on sub-scale microstructure) and the inherent flaw distribution [69]. For our foam materials, to identify a characteristic strain

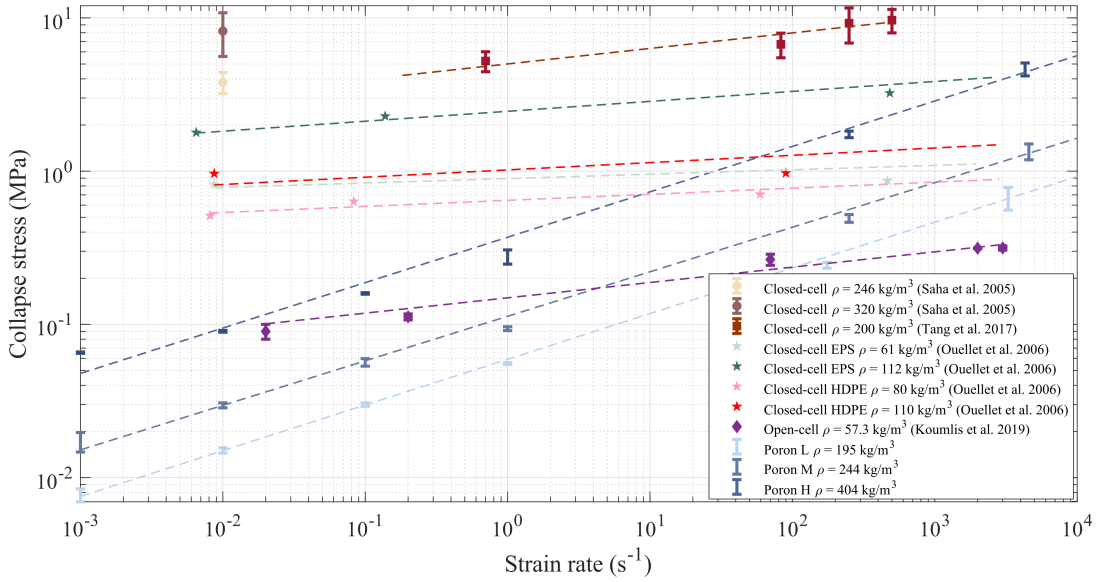

Fig. 9: Figure showing trends of collapse strength of different density foams with varying strain rates under compression loading. Data is ordered based on increasing density for a given study for open-cell foams, followed by closed cell foams. The y axis denotes the collapse stress (MPa) and the x axis represents strain rate (s^{-1}), and both the axes are represented in a logarithmic scale.

rate, more experiments at even higher strain rate conditions could be performed to guide when transitions between structural buckling (which is believed to dominate across our rates) and material yielding (which is believed to dominate at higher rates [54]). This could be coupled with numerical solutions that take into account geometry,damage, failure, and rate-effects in the base polymer. An analytical solution might be pursued, although these are believed to be to simplistic.

Next, β in equation (7) is the power-law coefficient, and this is dependent on the dominant mechanism, geometry, and material properties of the foam. In this study this value is derived from a curve fit ($\beta \sim 0.3$). From Figures 8 and 9, we can observe that this coefficient is not the same across all materials, and so a first principles solution to this value is likely challenging to generalize.

Finally, shown in Figure 10 is the resulting normalized σ_{pl}/E_0 for the three density

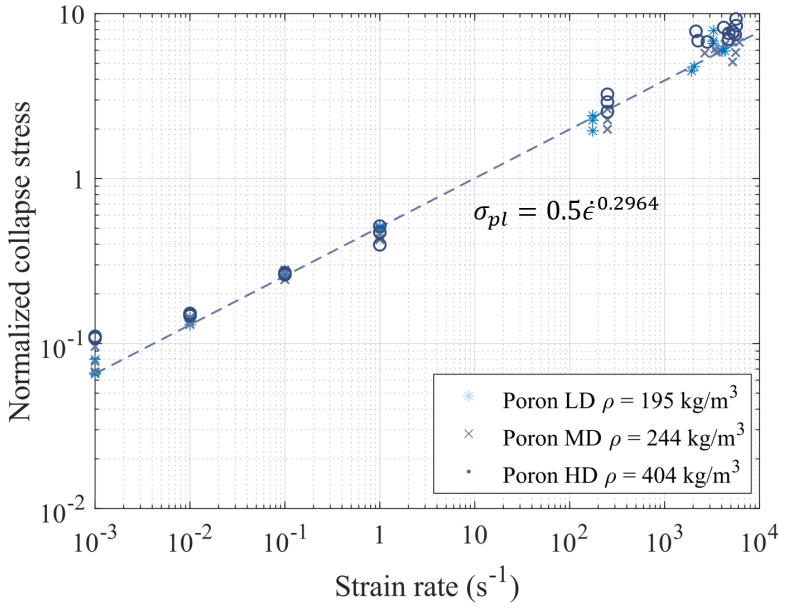

Fig. 10: Figure showing normalized collapse stress of different density foams with varying strain rates under compression loading.

foams from the present study. Note that the x axis is plotted in strain rate because no sufficient normalizing terms for $\dot{\epsilon}_0$ could be determined. From the figure, it is observed that the normalizing form provides sufficient collapse for the σ_{pl}. These concepts should be extended in the future to other foams to better generalize the approach and determine the coefficients.

6. Conclusion

The effect of density, microstructure and strain-rate on compressive response was explored for an open-cell polyurethane foam with varying densities of $195kg/m^3$, $244kg/m^3$, and $405kg/m^3$. Important microstructural parameters like pores sizes ($5\mu m$ to $145\mu m$) and wall thicknesses ($2\mu m$ to $23\mu m$) have been identified using Micro XCT and image processing techniques. Scaling laws to predict the effects of density and strain rate on

collapse stress (σ_{pl}) have been developed. The variation of the foam's characteristic properties (i.e., elastic modulus (E), collapse stress(σ_{pl}), with respect to strain rate are expressed in terms of the characteristic property value at the reference strain rate. These properties are found to behave in a power-law fashion with respect to strain rate. The observations and inferences are supported by stress-strain curves, XCT images of pristine microstructures, and eCDFs of pore sizes and wall thicknesses. The authors believe that the data and curve fits to analytical equations developed in this study will serve as a good starting point for impactful modeling of such materials [10, 53] that predict the effect of microstructure, density, and strain rate on the mechanical response of polymeric foams.

7. Acknowledgments

This research was sponsored by the Army Research Laboratory and was accomplished under Cooperative Agreement Number W911NF-16-2-0083. The views and conclusions contained in this document are those of the authors and should not be interpreted as representing the official policies, either expressed or implied, of the Army Research Laboratory or the U.S. Government. The authors also acknowledge Michael Harr and Paul Moy from US Army Research Laboratory for their help with experimentation. The U.S. Government is authorized to reproduce and distribute reprints for Government purposes notwithstanding any copyright notation herein. Research described in this paper was performed at the BMIT facility at the Canadian Light Source, which is supported by the Canada Foundation for Innovation, Natural Sciences and Engineering Research Council of Canada, the University of Saskatchewan, the Government of Saskatchewan, Western Economic Diversification Canada, the National Research Council Canada, and the Canadian Institutes of Health Research. We also greatly acknowl-

edge the in-kind support of Defence Research and Development Canada. We also thank Mitul Patel of Department of Mechanical Engineering, University of Alberta for his help with experimental setup.

8. Conflict of Interests

The authors declare that they have no conflict of interest.

9. References

References

[1] B. M. Patterson, N. L. Cordes, K. Henderson, J. J. Williams, T. Stannard, S. S. Singh, A. R. Ovejero, X. Xiao, M. Robinson, and N. Chawla, "In situ X-ray synchrotron tomographic imaging during the compression of hyper-elastic polymeric materials," *Journal of Materials Science*, vol. 51, no. 1, pp. 171–187, 2015.

[2] A. Shukla, Y. D. Rajapakse, and M. E. Hynes, *Blast mitigation: Experimental and numerical studies*, A. Shukla, Y. D. S. Rajapakse, and M. E. Hynes, Eds. New York, NY: Springer New York, 2013, vol. 9781461472, no. March. [Online]. Available: http://link.springer.com/10.1007/978-1-4614-7267-4

[3] G. Subhash, Q. Liu, and X. L. Gao, "Quasistatic and high strain rate uniaxial compressive response of polymeric structural foams," *International Journal of Impact Engineering*, vol. 32, no. 7, pp. 1113–1126, jul 2006.

[4] W. Chen, F. Lu, and N. Winfree, "High-strain-rate compressive behavior of a rigid polyurethane foam with various densities," *Experimental Mechanics*, vol. 42, no. 1, pp. 65–73, 2002.

[5] R. Bouix, P. Viot, and J. L. Lataillade, "Polypropylene foam behaviour under dynamic loadings: Strain rate, density and microstructure effects," *International Journal of Impact Engineering*, vol. 36, no. 2, pp. 329–342, feb 2009. [Online]. Available: http://linkinghub.elsevier.com/retrieve/pii/S0734743X08000791

[6] L. Cui, S. Kiernan, and M. D. Gilchrist, "Designing the energy absorption capacity of functionally graded foam materials," *Materials Science and Engineering A*, vol. 507, no. 1-2, pp. 215–225, 2009.

[7] T. a. Schaedler, a. J. Jacobsen, A. Torrents, a. E. Sorensen, J. Lian, J. R. Greer, L. Valdevit, and W. B. Carter, "Supplementary-Ultralight Metallic Microlattices," *Science*, vol. 334, no. 6058, pp. 962–965, 2011.

[8] J. Fitek and E. Meyer, "Design of a helmet liner for improved low velocity impact protection."

[9] M. Avalle, G. Belingardi, and R. Montanini, "Characterization of polymeric structural foams under compressive impact loading by means of energy-absorption diagram," *International Journal of Impact Engineering*, vol. 25, no. 5, pp. 455–472, 2001.

[10] L. Di Landro, G. Sala, and D. Olivieri, "Deformation mechanisms and energy absorption of polystyrene foams for protective helmets," *Polymer Testing*, vol. 21, no. 2, pp. 217–228, 2002.

[11] M. C. Saha, H. Mahfuz, U. K. Chakravarty, M. Uddin, M. E. Kabir, and S. Jeelani, "Effect of density, microstructure, and strain rate on compression behavior of polymeric foams," *Materials Science and Engi-*

neering A, vol. 406, no. 1-2, pp. 328–336, oct 2005. [Online]. Available: http://linkinghub.elsevier.com/retrieve/pii/S0921509305006830

[12] S. Ouellet, D. Cronin, and M. Worswick, "Compressive response of polymeric foams under quasi-static, medium and high strain rate conditions," *Polymer Testing*, vol. 25, no. 6, pp. 731–743, sep 2006. [Online]. Available: http://linkinghub.elsevier.com/retrieve/pii/S0142941806000973

[13] I. M. Daniel, J. M. Cho, and B. T. Werner, "Characterization and modeling of stain-rate-dependent behavior of polymeric foams," *Composites Part A: Applied Science and Manufacturing*, vol. 45, pp. 70–78, 2013. [Online]. Available: http://dx.doi.org/10.1016/j.compositesa.2012.10.003

[14] D. S. Cronin and S. Ouellet, "Low density polyethylene, expanded polystyrene and expanded polypropylene: Strain rate and size effects on mechanical properties," *Polymer Testing*, vol. 53, pp. 40–50, aug 2016.

[15] A. Ajdari, H. Nayeb-Hashemi, and A. Vaziri, "Dynamic crushing and energy absorption of regular, irregular and functionally graded cellular structures," *International Journal of Solids and Structures*, vol. 48, no. 3-4, pp. 506–516, 2011. [Online]. Available: http://dx.doi.org/10.1016/j.ijsolstr.2010.10.018

[16] J. Lankford and K. A. Dannemann, "Strain Rate Effects in Porous Materials," *MRS Proceedings*, vol. 521, pp. 103–108, 1998.

[17] J. Andersons, U. Cābulis, L. Stiebra, M. Kirpļuks, and E. Spārniņš, "Modeling the mode I fracture toughness of anisotropic low-density rigid PUR and PIR foams," *International Journal of Fracture*, vol. 205, no. 1, pp. 111–118, 2017.

[18] Q. Liu and G. Subhash, "A phenomenological constitutive model for foams under large deformations," *Polymer Engineering and Science*, vol. 44, no. 3, pp. 463–473, 2004.

[19] E. Linul, L. Marsavina, T. Voiconi, and T. Sadowski, "Study of factors influencing the mechanical properties of polyurethane foams under dynamic compression," *Journal of Physics: Conference Series*, vol. 451, no. 1, 2013.

[20] E. Linul, D. A. Şerban, L. Marsavina, and T. Sadowski, "Assessment of collapse diagrams of rigid polyurethane foams under dynamic loading conditions," *Archives of Civil and Mechanical Engineering*, vol. 17, no. 3, pp. 457–466, 2017.

[21] L. Marsavina, E. Linul, T. Voiconi, and T. Sadowski, "A comparison between dynamic and static fracture toughness of polyurethane foams," *Polymer Testing*, vol. 32, no. 4, pp. 673–680, jun 2013. [Online]. Available: http://dx.doi.org/10.1016/j.polymertesting.2013.03.013 https://linkinghub.elsevier.com/retrieve/pii/S0142941813000536

[22] J. Andersons, M. Kirpluks, L. Stiebra, and U. Cabulis, "Anisotropy of the stiffness and strength of rigid low-density closed-cell polyisocyanurate foams," *Materials and Design*, vol. 92, pp. 836–845, 2016.

[23] S. Koumlis and L. Lamberson, "Strain Rate Dependent Compressive Response of Open Cell Polyurethane Foam," *Experimental Mechanics*, may 2019. [Online]. Available: http://link.springer.com/10.1007/s11340-019-00521-3

[24] A. C. Kaya, P. Zaslansky, A. Nikolaus, and C. Fleck, "Tensile failure observations in sintered steel foam struts revealed by sub-micron contrast-

enhanced microtomography," *Materials and Design*, vol. 105, pp. 190–200, 2016. [Online]. Available: http://dx.doi.org/10.1016/j.matdes.2016.05.069

[25] S. Tammas-Williams, H. Zhao, F. Léonard, F. Derguti, I. Todd, and P. B. Prangnell, "XCT analysis of the influence of melt strategies on defect population in Ti-6Al-4V components manufactured by Selective Electron Beam Melting," *Materials Characterization*, vol. 102, pp. 47–61, 2015. [Online]. Available: http://dx.doi.org/10.1016/j.matchar.2015.02.008

[26] S. T. Methods, "Standard Test Methods for Flexible Cellular Materials — Slab , Bonded , and Molded Urethane Foams," *Astm*, vol. Designatio, no. January, pp. 1–29, 2012.

[27] "Poron XRD - extreme impact protection," p. 7843, 2009. [Online]. Available: http://www.poroncomfort.com/documents/2826/XRD-Standard-Physical-Properties.aspx

[28] A. D. 624-00, "Standard Test Method for Tear Strength of Conventional Vulcanized Rubber and," *Annual Book of ASTM Standards*, vol. 00, no. Reapproved, pp. 1–9, 2012.

[29] U. Jarfelt and O. Ramnäs, "Thermal conductivity of polyurethane foam - best performance Thermal conductivity of polyurethane foam Best performance," *10th International Symposium on District Heating and Cooling*, no. September, p. 12, 2006.

[30] L. J. Gibson and M. F. Ashby, "The Mechanics of Three-Dimensional Cellular Materials," *Proceedings of the Royal Society A: Mathematical, Physical and*

Engineering Sciences, vol. 382, no. 1782, pp. 43–59, jul 1982. [Online]. Available: http://rspa.royalsocietypublishing.org/cgi/doi/10.1098/rspa.1982.0088

[31] T. W. Wysokinski, D. Chapman, G. Adams, M. Renier, P. Suortti, and W. Thomlinson, "Beamlines of the biomedical imaging and therapy facility at the Canadian light source - Part 3," *Nuclear Instruments and Methods in Physics Research, Section A: Accelerators, Spectrometers, Detectors and Associated Equipment*, vol. 775, pp. 1–4, 2015.

[32] C. Lo, T. Sano, and J. D. Hogan, "Deformation mechanisms and evolution of mechanical properties in damaged advanced ceramics," *Journal of the European Ceramic Society*, vol. 40, no. 8, pp. 3129–3139, jul 2020. [Online]. Available: https://doi.org/10.1016/j.jeurceramsoc.2020.02.058 https://linkinghub.elsevier.com/retrieve/pii/S0955221920301667

[33] J. D. Hogan, L. Farbaniec, D. Mallick, V. Domnich, K. Kuwelkar, T. Sano, J. W. McCauley, and K. T. Ramesh, "Fragmentation of an advanced ceramic under ballistic impact: Mechanisms and microstructure," *International Journal of Impact Engineering*, vol. 102, pp. 47–54, 2017. [Online]. Available: http://dx.doi.org/10.1016/j.ijimpeng.2016.12.008

[34] M. E. Kabir, M. C. Saha, and S. Jeelani, "Tensile and fracture behavior of polymer foams," *Materials Science and Engineering A*, vol. 429, no. 1-2, pp. 225–235, 2006.

[35] T. Proulx, *Dynamic Behavior of Materials, Volume 1*, ser. Conference Proceedings of the Society for Experimental Mechanics Series, T. Proulx,

Ed. New York, NY: Springer New York, 2011. [Online]. Available: http://link.springer.com/10.1007/978-1-4419-8228-5

[36] R. Clamroth, "Determination of viscoelastic properties by dynamic testing," *Polymer Testing*, vol. 2, no. 4, pp. 263–286, oct 1981. [Online]. Available: https://linkinghub.elsevier.com/retrieve/pii/014294188190012X

[37] X. J. Wu and D. A. Gorham, "Stress Equilibrium in the Split Hopkinson Pressure Bar Test," *Le Journal de Physique IV*, vol. 07, no. C3, pp. C3–91–C3–96, 1997.

[38] B. Song, W. W. Chen, S. Dou, N. A. Winfree, and J. H. Kang, "Strain-rate effects on elastic and early cell-collapse responses of a polystyrene foam," *International Journal of Impact Engineering*, vol. 31, no. 5, pp. 509–521, 2005.

[39] W. W. Chen and B. Song, *Split Hopkinson (Kolsky) Bar*.

[40] B. Song, B. Sanborn, and W. Y. Lu, "Radial inertia effect on dynamic compressive response of polymeric foam materials," *Conference Proceedings of the Society for Experimental Mechanics Series*, pp. 85–87, 2019.

[41] K. B. Bhagavathula, A. Azar, S. Ouellet, S. Satapathy, C. R. Dennison, and J. D. Hogan, "High Rate Compressive Behaviour of a Dilatant Polymeric Foam," *Journal of Dynamic Behavior of Materials*, vol. 4, no. 4, pp. 573–585, dec 2018. [Online]. Available: http://dx.doi.org/10.1007/s40870-018-0176-0 http://link.springer.com/10.1007/s40870-018-0176-0

[42] G. T. Rusty, G. Iii, and W. R. Blumenthal, "Split-Hopkinson Pressure Bar Testing of Soft Materials," *Mechanical Testing and Evaluation*, vol. 8, pp. 488–496, 2018.

763 [43] Vic-2d, correlated solutions inc, irmo, south carolina, vic-2d. [Online]. Available:
764 https://www.correlatedsolutions.com/vic-2d/

765 [44] H. S. Michael A. Sutton, Jean Jose Orteu, *Image Correlation for Shape, Motion
766 and Deformation Measurements*. New York, NY: Springer US, 2009. [Online].
767 Available: https://www.springer.com/gp/book/9780387787466

768 [45] M. Sutton, J. Yan, V. Tiwari, H. Schreier, and J. Orteu, "The effect of out-of-plane
769 motion on 2d and 3d digital image correlation measurements," *Optics and Lasers
770 in Engineering*, vol. 46, no. 10, pp. 746 – 757, 2008. [Online]. Available:
771 http://www.sciencedirect.com/science/article/pii/S0143816608000985

772 [46] A. W. Van der Vaart, *Asymptotic statistics*. Cambridge university press, 2000,
773 vol. 3.

774 [47] Y. Sun and Q. M. Li, "Dynamic compressive behaviour of cellular materials: A re-
775 view of phenomenon, mechanism and modelling," *International Journal of Impact
776 Engineering*, vol. 112, no. October 2017, pp. 74–115, 2018.

777 [48] N. J. Mills, R. Stämpfli, F. Marone, and P. A. Brühwiler, "Finite element
778 micromechanics model of impact compression of closed-cell polymer foams,"
779 *International Journal of Solids and Structures*, vol. 46, no. 3-4, pp. 677–697,
780 2009. [Online]. Available: http://dx.doi.org/10.1016/j.ijsolstr.2008.09.012

781 [49] S. Gaitanaros and S. Kyriakides, "On the effect of relative density on the
782 crushing and energy absorption of open-cell foams under impact," *International
783 Journal of Impact Engineering*, vol. 82, pp. 3–13, 2015. [Online]. Available:
784 http://dx.doi.org/10.1016/j.ijimpeng.2015.03.011

[50] B. Song, W. Chen, and D. J. Frew, "Dynamic compressive response and failure behavior of an epoxy syntactic foam," *Journal of Composite Materials*, vol. 38, no. 11, pp. 915–936, jun 2004. [Online]. Available: http://journals.sagepub.com/doi/10.1177/0021998304040552

[51] A. D. Brydon, S. G. Bardenhagen, E. A. Miller, and G. T. Seidler, "Simulation of the densification of real open-celled foam microstructures," *Journal of the Mechanics and Physics of Solids*, vol. 53, no. 12, pp. 2638–2660, 2005.

[52] D. Zenkert and M. Burman, "Tension, compression and shear fatigue of a closed cell polymer foam," *Composites Science and Technology*, vol. 69, no. 6, pp. 785–792, 2009.

[53] N. Mills, "Polyurethane foams: processing and microstructure," pp. 19–37, 2007. [Online]. Available: https://linkinghub.elsevier.com/retrieve/pii/B9780750680691500039

[54] N. J. Mills and H. X. Zhu, "The high strain compression of closed-cell polymer foams," *Journal of the Mechanics and Physics of Solids*, vol. 47, no. 3, pp. 669–695, 1999. [Online]. Available: http://linkinghub.elsevier.com/retrieve/pii/S0022509698000076

[55] M. S. Gholami, O. Doutres, and N. Atalla, "Effect of microstructure closed-pore content on the mechanical properties of flexible polyurethane foam," *International Journal of Solids and Structures*, vol. 112, pp. 97–105, 2017. [Online]. Available: http://dx.doi.org/10.1016/j.ijsolstr.2017.02.016

[56] K. C. Rusch, "Load–compression behavior of flexible foams," *Journal of Applied Polymer Science*, vol. 13, no. 11, pp. 2297–2311, 1969.

[57] M. Tang, G. Huang, H. Zhang, Y. Liu, H. Chang, H. Song, D. Xu, and Z. Wang, "Dependences of Rheological and Compression Mechanical Properties on Cellular Structures for Impact-Protective Materials," *ACS Omega*, vol. 2, no. 5, pp. 2214–2223, 2017.

[58] Z. Nie, Y. Lin, and Q. Tong, "Modeling structures of open cell foams," *Computational Materials Science*, vol. 131, pp. 160–169, 2017. [Online]. Available: http://dx.doi.org/10.1016/j.commatsci.2017.01.029

[59] W. Y. Jang, A. M. Kraynik, and S. Kyriakides, "On the microstructure of open-cell foams and its effect on elastic properties," *International Journal of Solids and Structures*, vol. 45, no. 7-8, pp. 1845–1875, 2008.

[60] J. J. Timothy and G. Meschke, "A cascade continuum micromechanics model for the effective elastic properties of porous materials," *International Journal of Solids and Structures*, vol. 83, pp. 1–12, apr 2016. [Online]. Available: https://linkinghub.elsevier.com/retrieve/pii/S0020768315005028

[61] D. Weaire, S. T. Tobin, A. J. Meagher, and S. Hutzler, "Foam Morphology," *Foam Engineering: Fundamentals and Applications*, pp. 5–26, 2012.

[62] H. Niknam and A. H. Akbarzadeh, "Thermo-mechanical bending of architected functionally graded cellular beams," *Composites Part B: Engineering*, vol. 174, no. February, p. 107060, 2019. [Online]. Available: https://doi.org/10.1016/j.compositesb.2019.107060

[63] A. Bagher Shemirani, R. Naghdabadi, and M. J. Ashrafi, "Experimental and numerical study on choosing proper pulse shapers for testing concrete

specimens by split Hopkinson pressure bar apparatus," *Construction and Building Materials*, vol. 125, pp. 326–336, 2016. [Online]. Available: http://dx.doi.org/10.1016/j.conbuildmat.2016.08.045

[64] M. Eynbeygui, J. Arghavani, A. H. Akbarzadeh, and R. Naghdabadi, "Anisotropic elastic-plastic behavior of architected pyramidal lattice materials," *Acta Materialia*, vol. 183, pp. 118–136, 2020. [Online]. Available: https://doi.org/10.1016/j.actamat.2019.10.038

[65] S. Deschanel, L. Vanel, N. Godin, E. Maire, G. Vigier, and S. Ciliberto, "Mechanical response and fracture dynamics of polymeric foams," *Journal of Physics D: Applied Physics*, vol. 42, no. 21, 2009.

[66] O. E. Petel, S. Ouellet, A. J. Higgins, and D. L. Frost, "The elastic-plastic behaviour of foam under shock loading," *Shock Waves*, vol. 23, no. 1, pp. 55–67, 2013.

[67] V. A. Kuzkin, "Structural model for the dynamic buckling of a column under constant rate compression," pp. 1–8, 2015. [Online]. Available: http://arxiv.org/abs/1506.00427

[68] D. Dattelbaum, D. Robbins, R. Gustavsen, S. Sheffield, D. Stahl, and J. Coe, "Shock compression of polyurethane foams," *EPJ Web of Conferences*, vol. 26, p. 02014, 2012. [Online]. Available: http://dx.doi.org/10.1051/epjconf/20122602014

[69] J. Kimberley, K. T. Ramesh, and N. P. Daphalapurkar, "A scaling law for the dynamic strength of brittle solids," *Acta Materialia*, vol. 61, no. 9, pp. 3509–3521, 2013. [Online]. Available: http://dx.doi.org/10.1016/j.actamat.2013.02.045

List of Figures

List of Tables